Marginal detachment zones: the fracture factories of ice shelves?

Christopher Miele[1], Timothy Bartholomaus[2,2], Ellyn Enderlin[3,3], and Christopher Miele[1]

[1]University of Idaho
[2]University of Texas at Austin
[3]Boise State University

December 1, 2022

Abstract

Along the lateral margins of floating ice shelves in Greenland and Antarctica, ice flow past confining margins and pinning points is often accompanied by extensive rifting. Rifts in zones of marginal decoupling ("detachment zones') typically propagate inward from the margins and result in many of Earth's largest calving events. Velocity maps of detachment zones indicate that flow through these regions is spatially transitioning from confined to unconfined shelf flow. We employ the software package \textit{icepack} to demonstrate that longitudinally decreasing marginal resistance reproduces observed transitions in flow regime, and we show that these spatial transitions are accompanied by near-margin tension sufficient to explain full-thickness rifts. Thus, we suggest that zones of progressive decoupling are a primary control on ice shelf calving. The steadiness of detachment zone positions may be a good indicator of ice shelf vulnerability, with migratory or thinning detachment zones indicating shelves at risk of dynamic speedup and increased fracture.

Marginal detachment zones: the fracture factories of ice shelves?

Chris Miele,[1] Timothy C. Bartholomaus,[1] Ellyn M. Enderlin [2]

[1]Department of Geological Sciences, University of Idaho, Moscow, ID, USA
[2]Department of Geosciences, Boise State University, Boise, ID, USA

Key Points:

- Many calving events originate as near-margin rifts as ice shelves flow beyond lateral obstructions or boundaries.
- Physical detachment from lateral obstructions is a major source of near-margin tension and fracture.
- Within these marginal detachment zones, thinning/changes to fracture patterns may presage shelf destabilization.

Corresponding author: Chris Miele, cmiele@uidaho.edu

Abstract

Along the lateral margins of floating ice shelves in Greenland and Antarctica, ice flow past confining margins and pinning points is often accompanied by extensive rifting. Rifts in zones of marginal decoupling ("detachment zones") typically propagate inward from the margins and result in many of Earth's largest calving events. Velocity maps of detachment zones indicate that flow through these regions is spatially transitioning from confined to unconfined shelf flow. We employ the software package *icepack* to demonstrate that longitudinally decreasing marginal resistance reproduces observed transitions in flow regime, and we show that these spatial transitions are accompanied by near-margin tension sufficient to explain full-thickness rifts. Thus, we suggest that zones of progressive decoupling are a primary control on ice shelf calving. The steadiness of detachment zone positions may be a good indicator of ice shelf vulnerability, with migratory or thinning detachment zones indicating shelves at risk of dynamic speedup and increased fracture.

Plain Language Summary

The massive icebergs released from the ice shelves of Greenland and Antarctica all originate from fractures in the ice. Fracture occurs where extensional stresses are great enough to break the ice. We observe that zones of extensive fracture tend to coincide with regions where shelf ice flows just beyond lateral confinements such as fjord walls or islands, and that the fractures accrued through such zones often result in icebergs. In this study, we show that the high stresses within these zones occur as a result of a loss of contact with features at ice shelf edges. We propose that the regions where sidewall or island contact is lost may be an important indicator of future iceberg calving and changes in larger-scale ice shelf stability.

1 Introduction to ice shelves

The floating ice shelves of the Greenland and Antarctic Ice Sheets have undergone dramatic change in the past two decades (Hill et al., 2017; Paolo et al., 2015). Of the twelve glaciers in Northern Greenland which had 20th century floating extensions, all but five have retreated into grounded or nearly-grounded regimes, with only three maintaining shelves longer than a few kilometers in length (Hill et al., 2018). Antarctic shelves have collapsed due to unprecedented meltwater loading (Banwell et al., 2013), and Thwaites Glacier has notably retreated into a slab-capsize calving style reminiscent of Greenland's nearly-grounded glaciers (Winberry et al., 2020). Speedup of glacier ice driven by thinning and retreat of ice shelves is common in Antarctica (Joughin et al., 2021). Globally, the retreat, thinning, and speedup of ice shelves is expected to continue in the coming decades (An et al., 2021; Joughin et al., 2021; Rückamp et al., 2019).

Ice shelves occupy the most extended reaches of an ice sheet, fully floating downstream of the grounding zone. Where an ice shelf is confined between sidewalls, or driven into an island or localized bedrock high (a "pinning point"), the shelf exerts backpressure, helping to stabilize the grounding zone upstream (Gudmundsson, 2013). Unconfined shelf ice, in contrast, has no solid features against which to produce friction and shear stress, and it typically provides no significant buttressing unless surrounded by perennial sea ice (Wearing et al., 2020). Only the loss of confined, buttressing shelf ice has the potential to drive dynamic speedup through the reduction of backpressure (Fürst et al., 2016; Gudmundsson et al., 2019). Because of potential impact of certain iceberg calving events on grounding zone dynamics, and because dynamics at the grounding zone are a significant source of uncertainty in sea-level rise projections (Robel et al., 2019; Fox-Kemper et al., 2021), a major interest in glacier modeling is to develop process-based explanations of brittle fracture and iceberg calving (Benn & Åström, 2018), especially near regions which provide buttressing.

Unconfined shelf ice is typically found downstream of any obstructions, beyond the last contact between the shelf and any sidewalls or pinning points. Therefore, the space connecting confined and unconfined shelf ice represents a region in delicate balance: fracture and damage (i.e., brittle failure) downstream might result in little or no dynamic speedup, while damage upstream might have a non-negligible dynamic effect. We refer to such intermediary regions as *detachment zones*. In this study, we theoretically investigate detachment zones, and we find that they are inherently prone to high stresses and damage. We highlight these zones as significant drivers of iceberg calving from ice shelves.

1.1 Detachment zones: definition and observations

As identified above, we define a detachment zone to be the region over which shelf ice loses contact with rigid lateral boundaries (i.e., the space over which shelf ice physically detaches from its surroundings). The lateral boundaries with which contact is lost may include sidewalls, islands, and local bedrock highs (see Figure 1). Defined this way, the detachment zone of an ice shelf can be understood as the boundary between unconfined and confined shelf ice. Since buttressing decreases away from geometric confinements, this zone can be roughly interpreted as the spatial transition between the passive and buttressing areas described by Fürst et al. (2016).

Detachment zones are commonly marked by series of lateral-cutting rifts (Figure 1). Because they open near the margins within zones of diminishing sidewall contact, these rifts appear to be distinct from those which open well within shear zones (Lhermitte et al., 2020) or those which open near the centerlines of ice shelves (see, for example, panel B from Figure 2 of Joughin et al. (2021)). Near-margin rifts through detachment zones have been observed previously; for example, Reeh et al. (2001) note the "characteristic sawtooth indented lateral margins" at 79 North, and Holdsworth (1974) describe the rifts at the Erebus Ice Tongue as "marginal teeth." We include both sites within Figure 1.

Timelapse sequences of the Greenland locations (see Supporting Information), demonstrate that these rifts open quasi-periodically from the margins within detachment zones. These observations give rise to the natural hypothesis that the rifts seen in Figure 1 are caused by the spatial decoupling of shelf ice from lateral features. Notably, Lipovsky (2020) recently found that rifts are especially unstable (i.e., they tend to grow) near zones where the margin loses shear strength, as within a detachment zone. The continued propagation of any pre-existing rifts through detachment zones, therefore, is already theoretically supported. A central aim of this manuscript is to provide a mechanism supporting a causal relationship between detachment zones and the initial formation of ice-margin lateral rifts (hereafter, "detachment rifts"). That is, beyond being conducive to the continued growth of any pre-existing rifts (Lipovsky, 2020), detachment zones cause new rifts to form. We approach this problem using the finite element modeling package *icepack* (Shapero et al., 2021) (see Section 2.2).

Detachment rifts typically propagate from the margins toward the centerlines (in some locations, they route upstream as they grow – see Figure 2 for an example of this). When calving occurs at glaciers in these settings, icebergs almost always calve along these detachment rifts, although the icebergs themselves may not be released for years after initial rift formation.[1] That is, the continued growth of detachment rifts often leads to terminus retreat via large calving events. However, although large calving events from

[1] Figure 1 in Alley et al. (2019) demonstrates the detachment zones at Petermann and Pine Island Glacier resulting in large icebergs. Iceberg A-68, which made headlines following its discharge from the Larsen C ice shelf in 2017, emerged through the detachment zone identified in our Figure 1, as demonstrated by Figure 1 in Larour et al. (2021). Personal observations show that the detachment rifts at Ryder, 79 North, and the Ronne Ice Shelf routinely produce major calving events (including iceberg A-76 from the Ronne Ice Shelf, which is currently touted as the world's largest iceberg).

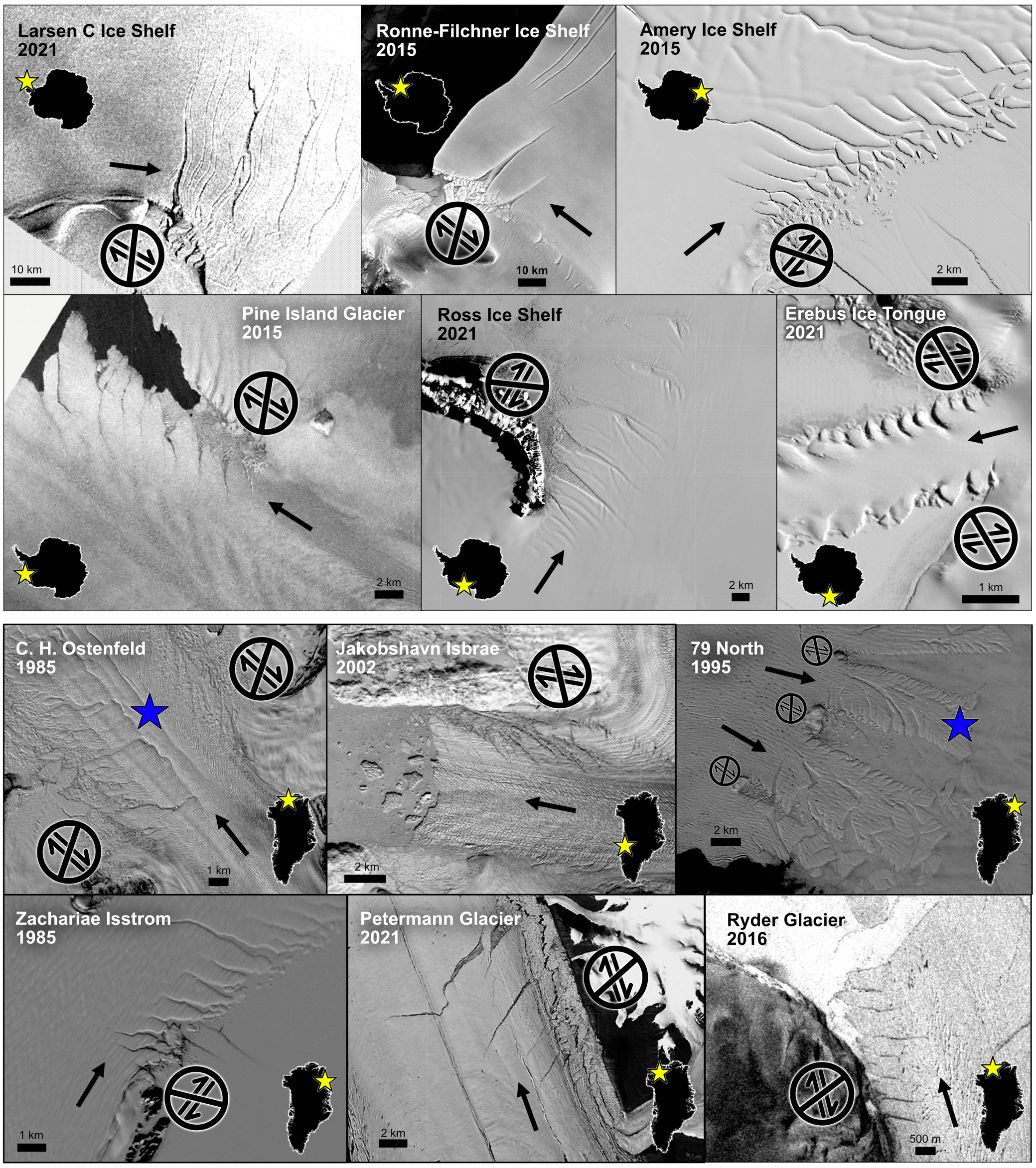

Figure 1. Detachment zones in Antarctica (top) and Greenland (bottom). No-shear symbols are oriented in the longitudinal direction and indicate the approximate locations where sidewall, island, or pinning point coupling is lost. Black arrows indicate flow direction, and insets indicate the location of each shelf. In all locations, series of near-margin rifts are present where shelf ice becomes uncoupled from lateral boundaries. The two Greenland locations on which our finite element simulations are based (C. H. Ostenfeld, and one of the middle tongues of 79 North) are marked with blue stars. All satellite imagery was obtained using the Google Earth Engine Digitisation Tool (Lea, 2018).

ice shelves tend to receive significant media attention, the initial formation of a rift may sometimes be more dynamically important than the resulting calving event itself. For example, in the area we identify as Petermann's detachment zone (see Figure 1), the initial formation of marginal rifts has been associated with speedup, while the actual discharge of icebergs is often dynamically unimportant (Rückamp et al., 2019).

2 Theory and modeling

2.1 An intuitive sketch of detachment zone dynamics

To test the mechanistic relationship between detachment zones and detachment rifting, we begin by providing a non-rigorous, yet intuitive sketch of how the loss of marginal resistance may result in the lateral rifting seen in Figure 1. We proceed to explore and test this sketch in Section 2.2.

The driving stress in confined shelf ice is resisted primarily by lateral shear stress, and, in unconfined shelf ice, primarily by gradients in longitudinal (along-flow) tension (Cuffey & Paterson, 2010). Therefore, the detachment zone couples two fundamentally different flow regimes, each of which is typified by a distinct velocity structure. The transverse velocity profile of a confined shelf is expected to be roughly quartic (see Equation 1), with a fast-moving centerline and slow-moving margins (van der Veen, 2013); the velocity profile of an unconfined shelf in uniaxial extension (i.e., if we consider the simplest-case scenario where lateral spreading is unimportant) is comparatively uniform in the transverse direction, with the margins moving at a rate similar to that of the centerline (Weertman, 1957). To transition from a confined regime to an unconfined regime across a nonzero space, the margins must speed up more than the centerline over the same distance; i.e., longitudinal strain rates must be greater at margins than at centerlines.

In glacier flow, extensional strain rates accompany tensile deviatoric stress (Cuffey & Paterson, 2010). Therefore, we expect that near-margin tension should emerge through detachment zones. Because tension is associated with fracture and rifting (Colgan et al., 2016), it is *a priori* reasonable to suppose that the presence of a detachment zone may explain the presence of near-margin rifts.

2.2 Finite element modeling with icepack

We use the flow modeling package *icepack* (Shapero et al., 2021) to solve the Shallow Shelf Approximation (SSA) (MacAyeal, 1989), with the intention of reproducing the transition in flow regime discussed above. We aim to demonstrate that a longitudinal decrease in lateral resistance produces near-margin tension sufficient to a) speed marginal ice up to centerline velocities, and b) open full-thickness rifts.

To this end, we model two distinct types of detachment zone. The first simulation is intended to approximate the detachment zone at C. H. Ostenfeld Glacier (OG), prior to the loss of its floating extension in the early 2000s. When OG's shelf was present, it emerged from between two roughly parallel sidewalls and poured into a wide embayment, losing wall traction as the fjord walls curved outward. The second simulation approximates the detachment zone at one of the protruding tongues still present near the middle of the 79 North Glacier ice shelf (79N), where the shelf approaches and then flows out from between two pinning points (see the location marked with the blue star in Figure 1). While both transitions fall under the definition of "detachment zone" given above, the dynamic changes experienced by OG and 79N are distinct. Velocity maps demonstrate that OG's upstream velocity profile is indicative of confined shelf flow with sidewall slip; upon flow through its detachment zone, the margins speed up to approach a more laterally uniform velocity profile (see Figure 2). This is a straightforward description of the discussion provided in Section 2.1. The tongue at 79N, in contrast, *begins* with a laterally uniform upstream velocity profile; upon approaching its pinning points, the margins slow down, only to speed back up again upon detachment from those pinning points (see Figure 3). The transition at OG is, in this sense, simple detachment, while the setting at 79N is two distinct transitions, "attaching" to its pinning points before detaching again.

Beyond typifying two complementary types of detachment zone, both OG and 79N have regular geometry relative to the large ice shelves found in Antarctica, allowing us to explore detachment zone dynamics in relatively simple, idealized scenarios. Moreover, both of the sites selected have historically extended several kilometers beyond their detachment zones (see the blue-starred images from Figure 1), making it easier to find velocity maps which cover the entire detachment zone; this is useful for model validation (see panel C from Figures 2 and 3).

2.2.1 Setup and boundary conditions

We employ icepack to solve the SSA, in which velocity and strain rates are uniform with depth (MacAyeal, 1989). We assume that neither OG nor 79N spread outward from the margins even where they are unconfined, although lateral flow is permitted *within* the domain (we justify this assumption in the final paragraph of this subsection). To roughly simulate both OG and 79N, we define the respective domains to be rectangular, with parallel sidewalls. The domain representing OG is 7.2 km in width and 10 km in length, and the domain representing 79N is 3.4 km in width and 6 km in length. OG is meshed with 200 m quadratic triangular elements. Due to its smaller size, we mesh 79N with a 100 m triangular grid. For each simulation, boundary conditions are required at the two sidewalls, the upstream boundary, and the downstream boundary.

At both OG and 79N, the downstream boundary condition is taken to be the terminus, at which the ice overburden is balanced by the pressure of seawater. Although the true tongue of 2000-era OG extended well beyond 10 km, the tongue was unconfined beyond this point, and the depth-averaged stresses within an unconfined tongue are governed by the same physics describing the depth-averaged stresses at the terminus (Weertman, 1957). Thus, additional simulation of the floating tongue should have no impact on stresses within the detachment zone (Figure 6 supports this).

The upstream boundary at OG is assumed to follow the theoretic velocity profile of a confined ice shelf resisted entirely by lateral shear (van der Veen, 2013). That is, there is no lateral velocity component, and the longitudinal velocity component, u_x, is given as a function of the transverse coordinate y. With the centerline velocity denoted u_c and W the half-width of the glacier, the appropriate description of u_x is

$$u_x(y) = u_c\left(1 - \left(\frac{y}{W}\right)^{n+1}\right), \tag{1}$$

where we assume the flow exponent n to take the conventional value of three (Cuffey & Paterson, 2010). The upstream centerline velocity u_c is informed by observations of early-2000s OG to be 500 m yr^{-1}. Although velocity data at OG demonstrate significant marginal slip at the upstream boundary (see Figure 2), we consider Equation 1 a sufficient approximation for the purposes of qualitatively reproducing detachment zone dynamics. The upstream boundary at 79N, as well, is taken to have no lateral velocity component. Its longitudinal velocity component is set at a laterally uniform 300 m yr^{-1}, which is representative of 2016 velocities at 79N.

Boundary conditions at the sidewalls are the key parameter in describing detachment zone dynamics. Here, we employ icepack's built-in sidewall boundary condition. By specifying the margins at both OG and 79N to be sidewalls, we guarantee that there is no lateral flow at the margins, while relating longitudinal velocity to frictional shear stress, τ_S, via a Weertman-type sliding law of the form

$$\tau_S \propto -C_f|\mathbf{u}|^{\frac{1}{m}-1}\mathbf{u}, \tag{2}$$

where C_f is the coefficient of sidewall friction, $m = 3$, and $\mathbf{u}$ is the velocity vector (Shapero et al., 2021). In its default application of the sidewall boundary condition, icepack takes C_f to be a spatially uniform, user-specified input. We modify icepack's sidewall friction law to allow for a spatially variable coefficient of sidewall friction. To approximate dynamics at OG, we set C_f to continuously diminish as the right half-period of a cosine curve, over the middle 2 kilometers of the longitudinal profile (see Figure 2). Upstream of the 2 km detachment zone, the coefficient of sidewall friction attains a longitudinally uniform baseline value, and beyond the detachment zone, it is uniformly zero (see Figure 2). We intend this 2 km dropoff in sidewall friction to reasonably approximate the loss of sidewall contact as the fjord walls curve away from direct contact with the shelf. We set the friction coefficient's baseline value, C_0, to 0.05, finding this value to produce reasonable model output – much higher, and the upstream stress profile becomes unphysically compressive with accumulated backpressure; much lower, and the sidewalls offer negligible resistance to flow, resulting in a simple, uniaxially extending shelf.

To approximate dynamics at 79N, we use a smaller baseline coefficient of sidewall friction, $C_0 = 0.025$, which we find to best reproduce the observed slowdown upon passage between the modeled pinning points (see Figure 3). We set the sidewall friction to rise to C_0 from zero, and then descend back to zero, across the middle 2 km of the profile as one full period of a cosine curve (see Figure 3). This 2 km period is chosen to match the 2 km transition zone implemented at OG. By our stated definition, only the final 1 km of the region with variable sidewall friction at 79N is a detachment zone, while the full 2 km transition zone at OG is a detachment zone.

Other combinations of boundary conditions may also plausibly simulate detachment zone dynamics. For example, at both OG and 79N, downstream of detachment, both shelves must be spreading laterally, since their sides are unconfined. It is possible to impose a floating ice cliff boundary condition at the lateral margins downstream of detachment to account for this lateral spread (similar to the floating ice cliff boundary condition used at the terminus). However, it is unclear to us how to impose a *gradual* transition from a confined flow regime to a biaxial spreading regime. We might prescribe an instantaneous transition from no-slip sidewalls to a laterally spreading margin at a "detachment point." However, we reason that, from a physical perspective, any transition between distinct flow regimes probably takes place over some nonzero distance. Therefore, we opt to treat detachment zones as the transition (over nonzero distance) from high-friction sidewalls to slippery sidewalls, even though treating the unconfined margins as slippery sidewalls precludes any lateral spread at these boundaries. Nonetheless, we find that the broad dynamic trends through our modeled detachment zones are robust to the choice of boundary condition transition, even when the transition is abrupt, as in the "detachment point" scenario described above. In the Supporting Figure S1, we demonstrate the qualitative similarity of results from different boundary condition setups.

2.2.2 Model spin-up

Given the setup described above, we advance each model forward in time to relax the idealized geometrical restrictions, described next. We solve the SSA iteratively, beginning with uniform-thickness shelves. We choose an initial surface elevation of 60 m for OG (informed by the historical DEM of Korsgaard et al. (2016)), and 10 m for 79N (as estimated via ArcticDEM). Velocity boundary conditions are those described in the previous section. Given velocity solutions from this first time step, a nonuniform thickness distribution is calculated, and the SSA is solved again. For simplicity, we assume

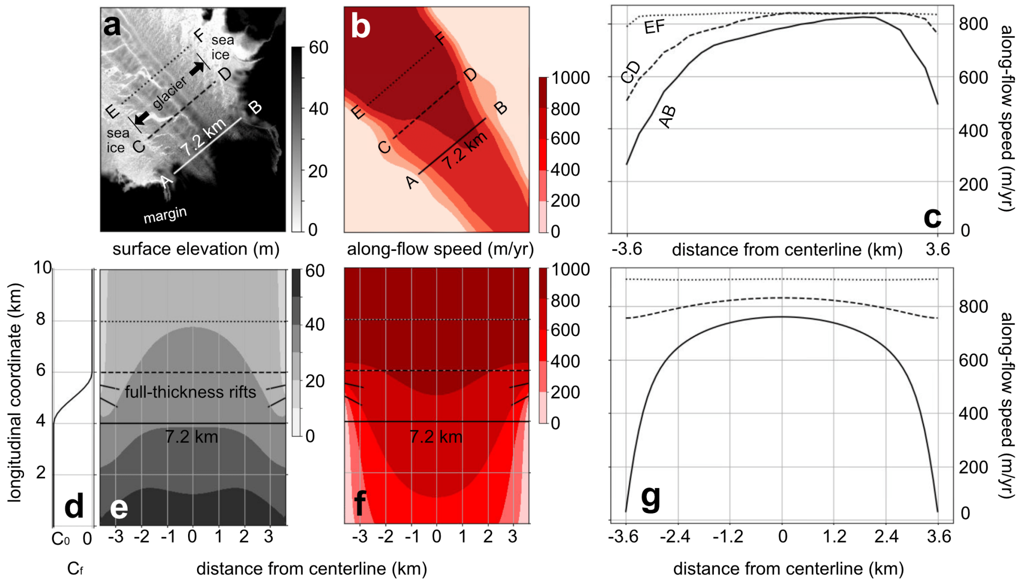

Figure 2. Surface elevation and velocity observations at OG (above), compared with model output (below). (a): 1978 surface elevation map (Korsgaard et al., 2016), with lateral profiles AB, CD, and EF bounding an approximately rectangular section of the shelf; (b): 2000-2001 mean annual along-flow speed (Mouginot et al., 2019); (c): Speed profiles along AB, CD, and EF. Over the space in which detachment rifts visibly form, the margins of OG speed up relative to the centerline. (d): The coefficient of sidewall friction, C_f, decreases longitudinally from baseline C_0 to 0 through the 2 km. (e): The steady-state surface elevation profile at OG produced by icepack. (f): The steady state velocity profile at OG. (g): velocity profiles along representative transverse profiles.

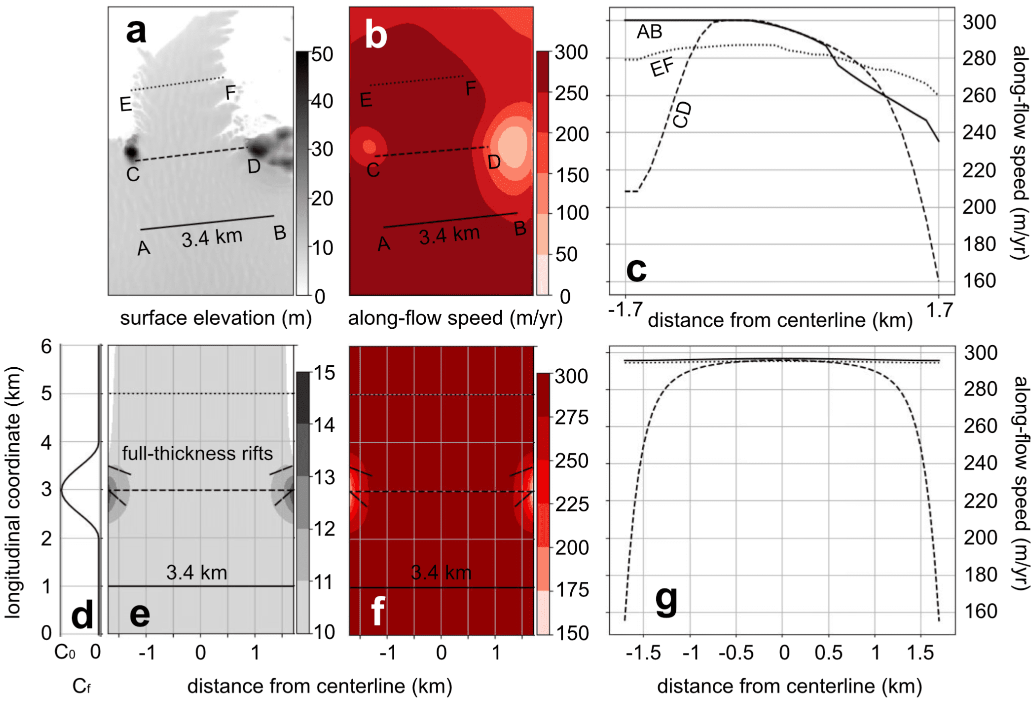

Figure 3. Surface elevation and velocity observations at 79N (above), compared with model output (below). (a): 2016 ArcticDEM surface elevation map, with lateral profiles AB, CD, and EF; (b): 2016 average along-flow speed (Mouginot et al., 2019); (c): speed profiles along AB, CD, and EF. Over the space in which detachment rifts visibly form, the margins of 79N speed up relative to the centerline. (d): The coefficient of sidewall friction, C_f, ramps up from 0 to the baseline value of C_0, and then back down to 0 over 2 km. The latter 1 km is the detachment zone. (e): The steady-state surface elevation profile at 79N produced by icepack. (f): The steady state velocity profile at 79N. (g): velocity profiles along representative transverse profiles.

a specific mass balance of 0 m yr^{-1} surface elevation change, so that all surface elevation change is dynamic. We iterate the solution step until the difference in mean thickness, from one iteration to the next, is less than 0.1% (we find that 100 years of simulated time is more than sufficient to produce this).

2.2.3 Rift locations and orientations

A major goal of this study is to demonstrate that the setup described above can produce full-thickness rifts like those shown in Figure 1. Therefore, our next step is to apply a fracture criterion to the output produced by icepack.

Once model experiments achieve steady-state, a post-processing step calculates strain rates, and, subsequently, deviatoric stresses by application of the standard constitutive relation (Cuffey & Paterson, 2010), with flow exponent $n = 3$ and icepack's rate factor for zero-degree, isothermal ice (Shapero et al., 2021). We assume that rifts form where surface crevasses penetrate through the full thickness of a shelf. The Nye zero stress criterion states that crevasses propagate to the depth at which the full longitudinal stress is zero (Nye, 1955). We adopt the natural 3-D generalization of this rule, suggested by Todd et al. (2018), wherein crevasses penetrate to the vertical coordinate at which the maximum tensile deviatoric stress (numerically calculated as the first eigenvalue of the deviatoric stress tensor) exactly balances the weight of the overlying ice column (i.e., the overburden pressure). Stated another way, this occurs when the net maximum tension is zero (Todd et al., 2018). Moreover, we assume that, where a crevasse reaches from the surface to the waterline, the process of hydrofracture ensures that the crevasse penetrates the rest of the way to the glacier base (O'Leary & Christoffersen, 2013). Therefore, we posit rifts to exist where the 3-D zero stress criterion yields a crevasse depth reaching sea level or deeper. In other words, rifts emerge where a) tension is sufficiently high, and b) the shelf is sufficiently thin, to drive a crevasse through the top 10% of a shelf's full thickness. In this 3-D implementation, crevasses open perpendicular to the direction of the maximum tensile stress (Colgan et al., 2016).

The Nye zero-stress criterion cannot account for the advection of crevasses away from the stress fields having initially opened them (Enderlin & Bartholomaus, 2020), and so this criterion is best used in locations where crevasses form locally, rather than being advected to their present location from afar. Our observations indicate that this is the case within detachment zones (see movies S1 through S4 in the Supporting Information). Moreover, the Nye criterion assumes densely-spaced crevasses, precluding stress concentration in crevasse tips (van der Veen, 2013). Because the crevasses which emerge through detachment zones are often spaced several local ice thicknesses apart, the Nye approach results in a conservative crevasse-depth estimate relative to a Linear Elastic Fracture Mechanics (LEFM) approach.

By invoking the process of hydrofracture, we additionally assume that there is a free connection between a crevasse and the ocean (Benn et al., 2007). We justify this assumption by noting that rifting through detachment zones occurs near the glacier margins where the ice is losing contact with any barriers which could otherwise prevent seawater from rushing in.

The approach to rift modeling outlined in this section is purely diagnostic; we do not attempt to include any dynamic effects of the modeled rifts. This could be accomplished, for example, by effectively softening the ice in response to fracture density (Vieli et al., 2006).

3 Model results

3.1 C. H. Ostenfeld

By choice of upstream boundary condition, the upstream boundary of OG has a transverse u_x velocity profile determined by Equation 1, with upstream centerline velocity 500 m yr^{-1}. In our modeled steady state profile of OG, stresses in the shelf become more tensile in the direction of flow, as compressive backpressure decreases toward the terminus (van der Veen, 2013). Centerline velocity steadily increases in the downstream direction, reaching a maximum of about 900 m yr^{-1} at the terminal boundary. The glacier margins, which are in firm sidewall contact at the upstream boundaries, begin to slip through the detachment zone, ultimately reaching velocities comparable to that of the centerline at the terminal boundary. Unlike the spatially gradual centerline speedup, the bulk of the marginal speedup occurs within the 2 km detachment zone. The magnitudes of the modeled velocities, and the trends followed by the modeled velocities, approximate the magnitudes and trends shown by velocity data at OG (see Figure 2), wherein the margins speed up disproportionately to match the centerline velocity.

The steady state elevation profile at OG exhibits a steady surface slope of about -0.004 along the centerline. Upstream of the detachment zone, the surface slope near the margin is comparable to that of the centerline. Through the detachment zone, however, near-margin longitudinal thinning is more pronounced, resulting in a near-margin surface slope of about -0.01 through the zone of sidewall detachment. This steep gradient levels off downstream of the detachment zone; by this point, marginal ice has thinned more than adjacent centerline ice.

The maximal value of the principal tensile stress is on the order of 200 kPa (see Figure 4, in which we depict modeled principal tension alongside the associated crevasse orientations and depths). This maximum occurs at the margins through the detachment zone, coinciding with the sharp speedup produced in these locations. Between the peak in tension and the pronounced thinning of the near-margin ice, the near-margin crevasses in the detachment zone reach the waterline. As a result of hydrofracture, the deepest crevasses penetrate the full thickness, emerging as marginal rifts through the detachment zone. These rifts are oriented toward the centerline and upstream, attaining strike angles from nearly-flow-perpendicular to about 45 degrees (see Figures 2 and 4).

3.2 79 North tongue

In this second experiment, we have chosen 79N's upstream boundary condition to be a laterally uniform 300 m yr^{-1}. In the along-flow direction, centerline velocity remains nearly uniform from the upstream boundary to the terminus, as the shelf is too thin to produce much extension. As the modeled pinning points are approached, near-margin velocity nearly halves, reaching 160 m yr^{-1} at the longitudinal midpoint of the domain, where the friction coefficient attains its maximum. Downstream, through the 1 km detachment zone, the margins speed up again, ultimately matching the centerline velocity by the end of the domain. The bulk of the near-margin slowdown, and subsequent speedup, occurs within the 2 km zone of variable sidewall friction.

The steady state surface elevation profile at 79N remains nearly level, with a small surface elevation gradient on the order of -0.001 at the centerline. Near the margins, however, small mounds of local thickening emerge where sidewall friction increases. Downstream of these local thick spots, as sidewall friction tapers back off, the shelf abruptly thins in the longitudinal direction, with the thinnest ice found near the margins through and beyond the detachment zone.

The maximal value of the first principal deviatoric stress is on the order of 150 kPa, and this maximal value is attained at either margin through the zone of marginal decoupling (see Figure 4). Full-thickness rifts, once more, are produced at the margins through the detachment zone, where tension is at its highest and thickness is at its lowest. The rifts are oriented inward and upstream to varying degrees: those emerging near the end of the detachment zone are nearly flow-perpendicular, while those emerging near the beginning of detachment intersect the margin at about 45 degrees.

4 Discussion

4.1 The fundamental detachment mechanism

We have outlined two key observations of detachment zones. First, as floating shelf ice flows beyond rigid, lateral features, the flow profile transitions from confined shelf flow (obeying Equation 1) to unconfined shelf flow (comparatively uniform in the transverse direction). Second, series of inward-cutting, lateral rifts emerge from the margins of detachment zones. In the context of glacier flow, both speedup and rifting are typically associated with tension within a shelf, and our finite element simulations produce tension sufficient to qualitatively explain both observations. Since spatially variable sidewall coupling is the only atypical detail of our setup, we have shown there to be a mechanistic link between sidewall detachment and tension in ice shelves. We conclude that the loss of sidewall friction over a shelf's domain results in a transition in flow profile, from confined to unconfined shelf flow, and that the tension and thinning arising through this transition zone is sufficient to open full-thickness rifts near the margins.

We posit the following fundamental detachment mechanism. Where near-margin ice is firmly connected to a rigid boundary, the coupling between centerline ice and marginal ice produces lateral shear stress. However, as that firm sidewall connection begins to weaken, fast-moving centerline ice pulls the slow marginal ice along, simultaneously increasing longitudinal tension while decreasing the centerline-margin velocity differential that produces lateral shear. Our finite element modeling demonstrates that this mechanism produces tension sufficient to speed marginal ice up to centerline velocities over the space of a few kilometers, while opening full-thickness rifts.

4.1.1 Contrasts between detachment zone types

In this study, we have modeled two distinct styles of marginal decoupling using a single, unifying approach. At locations like OG, the shelf simply loses contact with its confining sidewalls as it flows – for brevity, we refer to this situation as "simple detachment." In contrast, shelves like 79N first approach, and then flow outward from between, pinning points. Although the velocity and rifting profile of a shelf upon detachment from a pinning point (e.g., panel f of Figure 3) is similar to that of a shelf undergoing simple detachment (e.g., panel f of Figure 2), it is worthwhile to identify some contrasts between these two situations.

A key difference between simple detachment and pinning point detachment lies in the positioning of the relevant obstacles or boundaries. Pinning points are often not true islands, but local bedrock highs, or ice rises, where the shelf becomes locally grounded. For example, panel a of Figure 3 shows that, at the pinning points, the observed shelf elevation at 79N increases by up to 40 meters, indicating that the shelf is being pushed up and over local bedrock highs. Therefore, unlike in simple detachment from fjord walls, the resistance between a shelf and a pinning point may be more appropriately characterized by basal resistance, rather than lateral resistance. Below, we support the validity of treating this basal resistance as lateral resistance.

Velocity measurements show that ice rises slow the immediately overlying ice, producing a transverse velocity profile similar to that arising from lateral drag (see profile CD in panel c of Figure 3). In this situation, basal resistance from the ice rises is the cause of the emergent lateral drag. Since the assumptions underlying the SSA likely break down where there is significant basal drag, we do not attempt to model flow directly atop the ice rises. Instead, we restrict our modeled domain to ice that is fully floating between the ice rises, and we model the lateral drag alone as sidewall friction. As such, modeled increases in surface elevation near pinning points (see panel e of Figure 3) are due to dynamic thickening of the shelf and are much smaller than the 40-meter increase as the observed shelf is driven up and over the bedrock highs. However, we find that qualitatively similar results to those in Figure 3 are produced when we model ice rises in terms of basal resistance using the Shallow Stream Approximation (MacAyeal, 1989), in which basal resistance is assumed to be accommodated primarily by membrane stresses (see Supporting Figure S2).

4.2 Detachment rift morphology

The rifts which emerge near the margins of observed detachment zones tend to cut inward and slightly upstream, with typical strike angles ranging from about 45 degrees to flow-perpendicular (see Figure 1). Although many detachment rifts propagate no more than several hundred meters from the glacier margin, those that propagate further often curve more sharply upstream with distance from the sidewall (see 79 North from Figure 1, for example). Rifts which propagate even further toward the centerline may arc back, tending toward a flow-perpendicular orientation, once more, as they approach the middle of the shelf (see Supplementary Movies S1 through S4).

The locations and orientations of our modeled rifts are in reasonable agreement with these observations, although the rifted area is somewhat larger in the observations than the models. This underestimate in the model results is expected from our use of the conservative Nye crevasse depth criterion, which, as discussed previously, assumes a dense crevasse field and does not account for rift growth. We note that, once formed, rifts through detachment zones are likely to be unstable and propagate further (Lipovsky, 2020). Our modeled rifts cut inward and upstream, with strike angles ranging from about 45 degrees to nearly flow-perpendicular. In particular, rifts which form near the onset of detachment are closer to 45 degrees, while those which form toward the downstream end of detachment are closer to flow-perpendicular (see Figure 4). This is in good agreement with the observation that, where sidewall friction is strong, crevasses emerge at a 45 degree angle to the wall (Colgan et al., 2016), whereas in uniaxial extension regimes, crevasses should be flow-perpendicular.

Although we model only steady-state stress fields, it is common to assume that rifts tend to propagate along contours normal to the principal tension (Hulbe et al., 2010; De Rydt et al., 2018, 2019). Since the crevasses shown in Figure 4 are normal to the principal tension, a propagating detachment rift would likely tend to follow the depicted field of crevasse orientations. By this estimation, we find that the rifts emerging from the downstream extent of a detachment zone will begin fairly flow-perpendicular, cut more sharply upstream, and then cut less steeply across the glacier to cross the centerline at a flow-perpendicular angle. Rifts which form further upstream within the detachment zone start near 45 degrees, and become increasingly flow-perpendicular as they approach the centerline. In the case of pinning points (panel A of Figure 4), additional deep crevasses or even rifts may emerge through the zone where sidewall friction is increasing (as opposed to decreasing, as in a detachment zone). These crevasses can approach a flow-parallel orientation; we discuss these rifts below.

4.2.1 Rift formation upstream of detachment zones

The theoretical mechanism by which upstream-cutting rifts can form upon *approach* of a pinning point is the longitudinal compression emerging from the longitudinal increase of lateral shear. As shown in Figure 3, as a pinning point is approached, the margins of

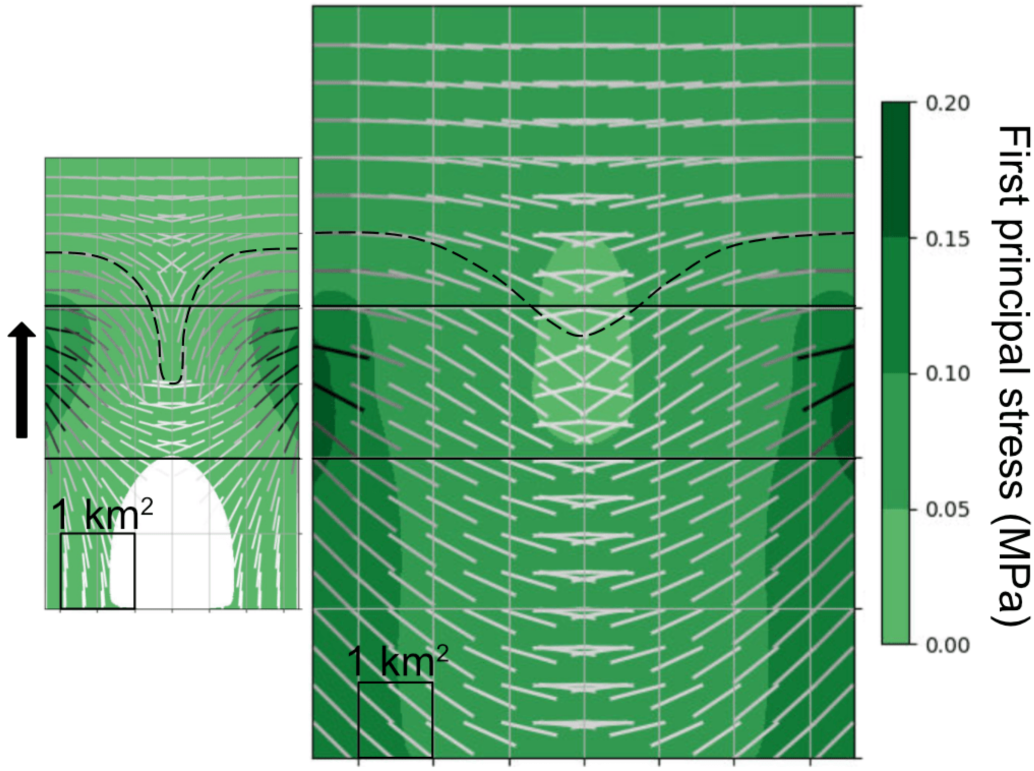

Figure 4. Steady state first principal stress magnitudes and rift orientations at both 79N (left) and OG (right). In both cases, the first principal stress attains its maximum near the margins, where sidewall coupling drops off. The solid, black, transverse lines indicate the regions over which variable sidewall friction is imposed. Crevasse locations and orientations are indicated by line segments, with shading indicating the depths to which the crevasses penetrate. Black line segments are crevasses which reach the waterline (and, hence, qualify as full-thickness rifts), and white line segments indicate crevasses of nearly zero depth. Dashed lines are a rough representation of the trajectory a rift might take, were it to propagate across the width of the shelf. White space indicates regions over which flow is compressive. Black arrow indicates flow direction.

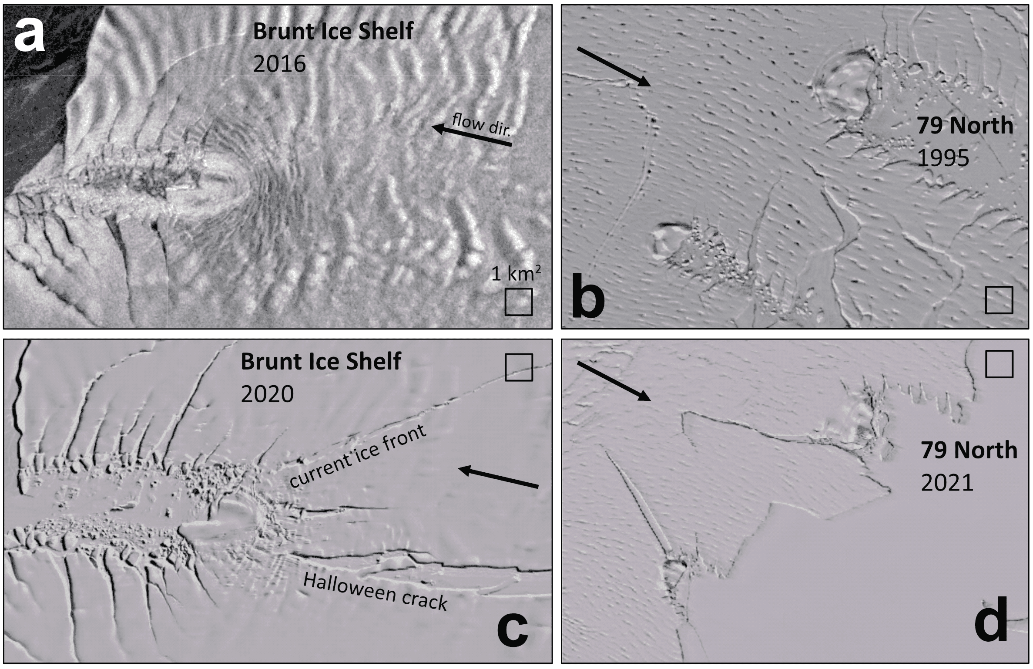

Figure 5. Recent changes to the rift profile of the Brunt Ice Shelf (75.45 S, 26.34 W) and one of the tongues of 79 North Glacier (79.47 N, 19.71 W). Panels (a) and (b) show, respectively, the rifts previously emerging as the Brunt Ice Shelf and 79 North pass pinning points: nearly flow-perpendicular rifts emerge as pinning point contact drops off. Panels (c) and (d) demonstrate the current rift profiles at Brunt and 79 North: at both sites, a new generation of nearly flow-parallel rifts have opened upstream of the pinning points. Squares are 1 km^2 scale markers.

a shelf slow down, exhibiting longitudinal compression. Because ice is incompressible, that longitudinal compression must be balanced by a combination of vertical and lateral tension. In this case, as Figure 4 demonstrates, the lateral tension dominates, so that the orientation of maximum tension, upstream of the pinning point, approximates the flow-perpendicular direction – this orientation gives rise to nearly flow-parallel crevasses. If the ice is sufficiently thin, the mechanism described above predicts the formation of full-thickness rifts, upstream of a pinning point, which are oriented approximately along-flow. This is a distinct mechanism from the detachment mechanism discussed previously, as it does not occur within detachment zones, but, instead, in locations where lateral resistance is longitudinally increasing. However, like the detachment mechanism, rifting is, in this case, related to zones of spatially variable side friction.

Observations of the Brunt Ice Shelf and 79 North Glacier corroborate the existence of a distinct mechanism inducing longitudinally-oriented rifts upstream of pinning points. Until recently, both the Brunt Ice Shelf and the 79 North Glacier ice shelf exhibited typical detachment rifting as they flowed beyond pinning points, with nearly-flow-perpendicular rifts cutting laterally upon detachment (see the top two panels of Figure 5). However, in the past decade the morphology of rifts at both sites has changed. Rifts currently form on the upstream side of the pinning points, cutting in the upstream direction (see the bottom panels), as described above.

These upstream-cutting rifts may poise a shelf to undergo dynamic changes. This is because, unlike true detachment rifts (which form as sidewall or pinning point contact is already being lost), these rifts form further upstream, where that lateral contact still supplies significant resistance. By damaging the ice upstream in this manner, this mechanism has the potential to reduce contact between shelf ice and pinning points, reducing buttressing, and thereby priming a shelf for speedup, dynamic thinning, and retreat. By this proposed paradigm, both the Brunt Ice Shelf and 79 North could be more vulnerable to dynamic speedup now then they were in the top panels of Figure 5.

4.3 The influence of detachment zone location on shelf dynamics

The analysis of Hindmarsh (2012) explored a transition zone closely related to detachment zones. In the language of Hindmarsh, the change in boundary conditions at a confined ice shelf's terminus (i.e., the transition from shearing sidewalls to a free ice cliff) gives rise to a *boundary layer*, in which flow spatially adjusts to a regime consistent with the terminal boundary. Hindmarsh (2012) investigated the boundary layer of a completely confined ice shelf terminating in a floating cliff (we illustrate this case in the first column of Figure 6). The finite element simulations we describe in Section 2.2 can be regarded as a generalization of the work of Hindmarsh: we consider the same shift from confined shelf flow to a terminal cliff, but we allow the shelf to gradually decouple from the sidewalls along the interior of the domain leading up to the cliff, while Hindmarsh does not. In this sense, Hindmarsh's modeled "detachment zone" occurs abruptly at the terminus, while we have prescribed ours to be upstream and of nonzero length.

Hindmarsh found that, as the flow regime shifted upon approach of the terminal boundary, there was an increase in tension near the two downstream corners of the domain. This finding is similar in character to our finding that high tension emerges through detachment zones. However, for Hindmarsh, the principal direction of the tension was found to be flow-perpendicular, which would give rise to flow-parallel crevasses. This is in contrast with our modeled crevasse orientations, which attain strike angles closer to flow-perpendicular (except upon the approach of pinning points, as discussed above). Because Hindmarsh's setup differs from ours only in the location over which sidewall resistance is lost, the contrast identified above raises the possibility that stresses within the boundary layer – and, therefore, the associated crevasse orientations and depths – may vary with the distance between a detachment zone and the terminus.

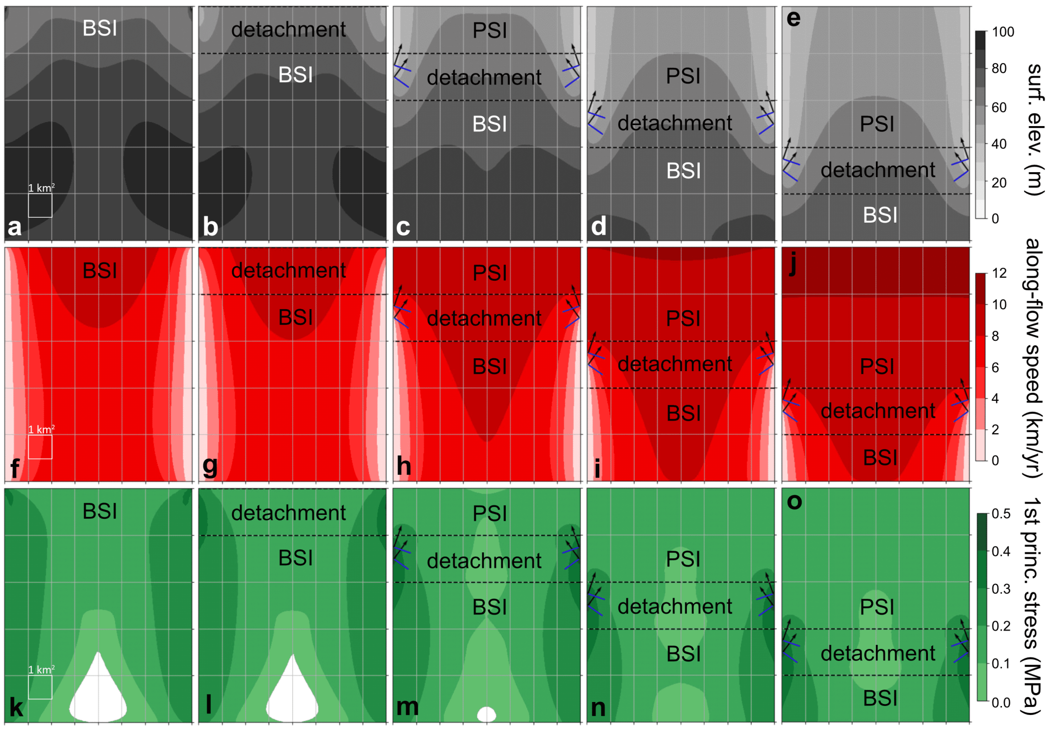

Figure 6. Five steady state surface elevation (a – e), speed (f – j), and first principal stress (k – o) descriptions. In the first column (a, f, k), the shelf does not detach from its sidewalls. In each subsequent column, a detachment zone is introduced at different distances upstream from the terminus, in increments of 2 km. Passive shelf ice (abbreviated to PSI in the figure), buttressing shelf ice (BSI), and detachment zones are marked. Where tension attains levels sufficient to open full-thickness rifts, the first principal stress orientation is shown by a black arrow, and the resulting rift is shown by a blue line.

To test the dependence of detachment zone behaviour on detachment zone location, we model five shelves of 10 km length, 8 km width, uniform 80 m surface elevation, and 800 m/yr centerline velocity at the upstream boundary (this configuration is chosen to approximate the 1990s floating ice tongue of Jakobshavn Isbrae, for reference with the next discussion point). The first shelf is firmly coupled to its sidewalls across its entire domain, which is the case considered in Hindmarsh (2012); the second detaches from its sidewalls between the 8 and 10 km mark; the third detaches between 6 and 8 km; the fourth, between 4 and 6 km; and the fifth, between 2 and 4 km (see Figure 6). Each detachment zone is prescribed as a decrease in sidewall friction in the gradual manner described in Section 2.2. That is, the only difference in setup between the five cases is the position of the detachment zone. The upstream velocity boundary condition is prescribed, in each case, to satisfy Equation 1 with a centerline velocity of 800 m/yr. We model each of the five shelves toward their steady state profiles, and we examine the steady state thickness, velocity, and principal tension (see Figure 6).

In the setup mimicking that of Hindmarsh (i.e., the first column of Figure 6), tension does peak near the downstream corners of the domain, as observed by Hindmarsh, but those stresses are insufficient to open full-thickness rifts under the depicted steady-state geometry. We find that rifts emerge only in those shelves with detachment zones contained fully within the interior of the domain (i.e., the three shelves with passive margins identified downstream of detachment). This suggests that detachment rifts are emergent features which occur only when a detachment zone is sufficiently removed from the terminus.

Moreover, it can be seen from Figure 6 that, the further back from the terminus a detachment zone is found, the thinner the steady-state geometry becomes, and the faster the shelf flows. This is consistent with the observation that, the further upstream a detachment zone is, the less buttressing the upstream shelf can provide. Essentially, as a detachment zone migrates upstream, buttressing shelf ice is replaced with passive shelf ice, which no longer provides resistance to flow. Although we have modeled only steady states, it is reasonable to suppose that the gradual formation and/or upstream retreat of a detachment zone may result in speedup, thinning, and fracture consistent with a progression from the leftmost panels to the rightmost panels of Figure 6. That is, a fully-coupled shelf/sidewall system, such as that depicted in panels a), f), and k), may reasonably evolve into the fast-flowing, rifted system shown in panels e), j), and o) upon the introduction of a detachment zone well upstream. We suggest that the upstream migration of detachment zones may indicate vulnerability of a shelf to increased fracture and calving.

As a corollary of this point, we caution against a potential misreading of Fürst et al. (2016). Fürst et al. (2016) describe the passive margin as a *safety band*, in the sense that ice shelf speedup resulting from damage to buttressing shelf ice only occurs "once calving exceeds the [passive] area." It would be possible to misinterpret this as suggesting that buttressing shelf ice is safe from damage until the passive area has been lost to successive calving events. However, such a reading would lead to an erroneous assessment of ice shelf stability. As we have simulated, damage most likely initiates in detachment zones upstream of an intact passive margin, regardless of how large that margin is (see especially the final column of Figure 6). Thus, we emphasize that the safety band of Fürst et al. (2016) should not be understood to inherently impart protection.

4.4 How do new detachment zones form?

The previous section illustrated how shelves with detachment zones in varying locations may dynamically differ from one another. Here, we consider how a detachment zone might form in the first place.

One of the most striking examples of detachment zone formation occurred at the northern sidewall of Jakobshavn Isbrae preceding the breakup of its shelf in the early 2000s. Jakobshavn is a Greenland outlet glacier of global importance; at the turn of the millennium, Jakobshavn alone accounted for about 4% of the rate of global sea-level rise (Joughin et al., 2004). From the late 90s to the early 2000s, Jakobshavn underwent a period of rapid thinning and speedup initiated by an influx of warm water beneath the shelf (Holland et al., 2008; Motyka et al., 2011).

Prior to 2000, Jakobshavn had firm sidewall contact, producing a typical confined shelf velocity profile with minimal longitudinal extension (see Panels D and E of Figure 7). By 2002, the northernmost shelf margin had visibly detached from the adjacent sidewall, and a series of rifts originate from this zone. Damage can effectively soften ice (Vieli et al., 2006; Albrecht & Levermann, 2012), and it has been suggested by Joughin et al. (2004) that the new marginal rifts at the edges of the shelf may have weakened the glacier margins. Marginal weakening (i.e., a decrease in lateral resistance between the glacier and its sidewalls) could have contributed to the speedup and retreat of the ice tongue via the reduction of backpressure (van der Veen et al., 2011).

We posit a different chain of events than in Joughin et al. (2004) and van der Veen et al. (2011). We suggest that, rather than rifts weakening the margins and leading to the shelf's collapse, the causation is in the other direction. By the analysis presented in this manuscript, the formation of the detachment zone at Jakobshavn (see panel B of Figure 7) indicates that the downstream extent of the northern margin must have weakened between 2000 and 2002. As shown in Figure 6, the introduction of a modeled detachment zone to a Jakobshavn-sized shelf can explain speedup, thinning, and rifting, of a similar scale to that observed prior to the total loss of the Jakobshavn ice tongue (Holland et al. (2008) report near-terminus thinning in the order of 300 meters preceding breakup – which corresponds to surface elevation lowering of about 30 meters – and velocity increases up to more than 12 km per year). That is, rather than rifts (formed for unspecified and unknown reasons) effectively weakening the margins, we suggest that marginal weakening reduced sidewall coupling and resulted in the formation of a detachment zone. Rifting then occurs via the detachment mechanism. The question, which we address in the next paragraph, then shifts from "What caused the rifting?" to "What caused the marginal weakening?" In this setting, we argue that it is, therefore, the new development of the detachment zone in the early 2000s, which preconditioned the shelf for collapse.

Between 1997 and 2003, the Jakobshavn ice tongue thinned in response to ocean forcing (Holland et al., 2008; Motyka et al., 2011). The strength of sidewall coupling varies in proportion with the area of ice-sidewall contact (Jordan et al., 2018), and so the thinning of a shelf should weaken the lateral margins. This initial marginal weakening, in turn, reduces backpressure, resulting in centerline speedup and increased lateral shear, exacerbating the thinning and weakening of the shear margins. A sufficiently weakened margin could result in the total decoupling of marginal ice from a lateral boundary, creating a detachment zone.

Further exacerbating this process is the possibility that ocean-induced thinning can preferentially erode the shear margins of ice shelves. The preferential erosion of shear margins can occur via several mechanisms (Jordan et al., 2018; Alley et al., 2019; Feldmann et al., 2022). When significant basal melt occurs in the grounding zones of ice streams like Jakobshavn, the fastest-flowing centerline ice is advected away from the region of heightened melt much more quickly than the much slower-moving shear margins. Thus, marginal ice is thinned more than centerline ice in response to the same forcing (Feldmann et al., 2022). This is compounded by dynamic thinning, as the fast centerline ice pulls and thins the relatively stagnant margins (Alley et al., 2019). Additionally, the coriolis force can direct currents to one side of a fjord system, resulting in enhanced melt beneath one shear margin (Goldberg et al., 2012; Jordan et al., 2018). Once a basal trough

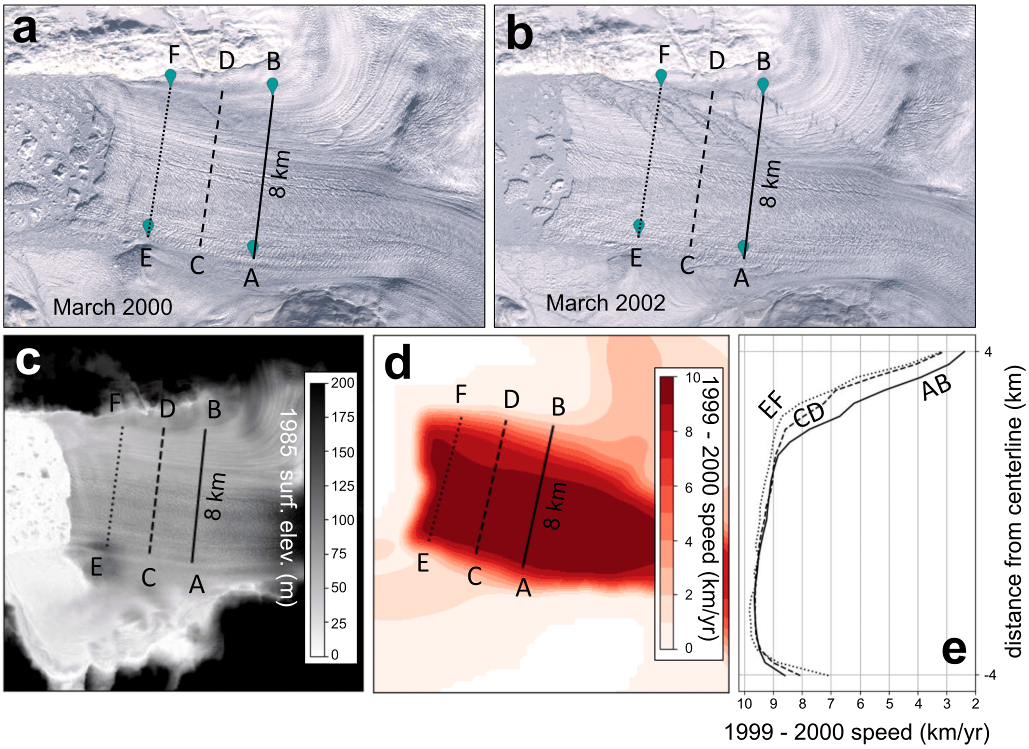

Figure 7. Jakobshavn Isbrae leading up to the loss of its ice shelf. Transverse profiles AB, CD, and EF are constant across all panels. (a): Satellite imagery of the Jakobshavn ice shelf in 2000, prior to its detachment zone development. (b): By 2002, the shelf had visibly detached from its northern sidewall, and detachment rifts had emerged. (c): A historical 1985 DEM of Jakobshavn (Korsgaard et al., 2016) demonstrates fairly level shelf geometry in the 80s. (d): Average along-flow speed (1999 – 2000) at Jakobshavn's ice tongue, prior to the introduction of its detachment zone, indicates little longitudinal extension. (e): 1999 – 2000 mean speed, evaluated along the indicated transverse profiles, indicates that the shelf at Jakobshavn was controlled by lateral shear up to the terminus, supporting the observation that Jakobshavn did not have a detachment zone in 2000.

has initially formed beneath a shear margin, that trough provides a natural channel for focusing buoyant, fresh, subglacial meltwater, which can increase melt by turbulent mixing (Carroll et al., 2016). All of these mechanisms may act in concert to create and sustain deep depressions at the shear margins, in some cases decoupling shelf ice from lateral boundaries (Goldberg et al., 2012; Feldmann et al., 2022), thereby creating detachment zones.

Looking beyond Jakobshavn, there does seem to be a correlation between shear margin troughs and detachment zone development. For example, basal mapping indicates that the detachment zone at Petermann (see Figure 1) is collocated with a deep shear margin trough where submarine melt is known to be high (Cai et al., 2017); the detachment zone we identify at Pine Island Glacier (also shown in Figure 1) is collocated with a persistent polynya, indicating that warm water is being channelized here (see Alley et al. (2019) for both observations). We suggest that preferential shear margin thinning may be a key driver of detachment zone formation, and that ocean forcing may, therefore, play an important role.

4.5 A sideways glance at grounding zones

Thus far, this manuscript has focused on the floating shelves of glaciers, where the driving stress is balanced by lateral shear stress and gradients in longitudinal tension. Further upstream, however, where the glacier becomes grounded, flow is often balanced largely by basal resistance (Schoof, 2007). The grounding zone, as the spatial transition from a grounded glacier to a floating ice shelf, couples two fundamentally different flow regimes across a space of a few kilometers (Tsai et al., 2015; Dawson & Bamber, 2020), in much the same way that a detachment zone couples confined shelf flow to unconfined shelf flow. The regime shift observed through detachment zones may, in this way, serve as an instructive analogy for the regime shift observed through grounding zones Hindmarsh (2012) essentially makes this very observation, with reference to the boundary layer connecting confined flow to the free ice cliff at the terminus.

The grounding zone is often visually identifiable from elevation or velocity data: as ice flows through the grounding zone, ice speeds up and thins, resulting in a conspicuous inflection in surface elevation, as well as high velocity gradients accompanied by basal fracturing (James et al., 2014; Murray et al., 2015; Wagner et al., 2016). Glaciers which terminate within the grounding zone (nearly-grounded glaciers) exhibit a unique style of iceberg calving, wherein the characteristic upward flexure results in full-thickness fracture of near-terminus ice, releasing outward-rotating icebergs (Amundson et al., 2008; Veitch & Nettles, 2012). We find it compelling that this style of basal fracture and iceberg release (following a loss of basal drag) resembles a vertical version of detachment zone fracture and rift-enabled calving (following a loss of lateral drag; see Figure 11 from Murray et al. (2015), and our Figure 8).

Given the uncertainty in long-term sea-level rise projections stemming from the possibility of unstable grounding zone feedbacks, accurately modeling the behaviour of glacier ice through the grounding zone is of primary concern in the glaciology community (Bamber et al., 2019; Robel et al., 2019; Schoof, 2007; Tsai et al., 2015). With the striking visual and theoretical similarities between detachment zone dynamics and grounding zone dynamics identified above, we suggest, as described in the next paragraph, that something similar to the detachment mechanism may help explain some of the emergent features through grounding zones.

Analogous to the intuitive argument presented earlier in this manuscript, a grounding zone represents a shift from significant basal resistance to a velocity regime dominated by membrane stresses. To transition from one flow regime to the other, the base of the glacier must speed up relative to the surface. That is, the base of the glacier must experience a higher longitudinal strain rate than the surface. Therefore, we expect that

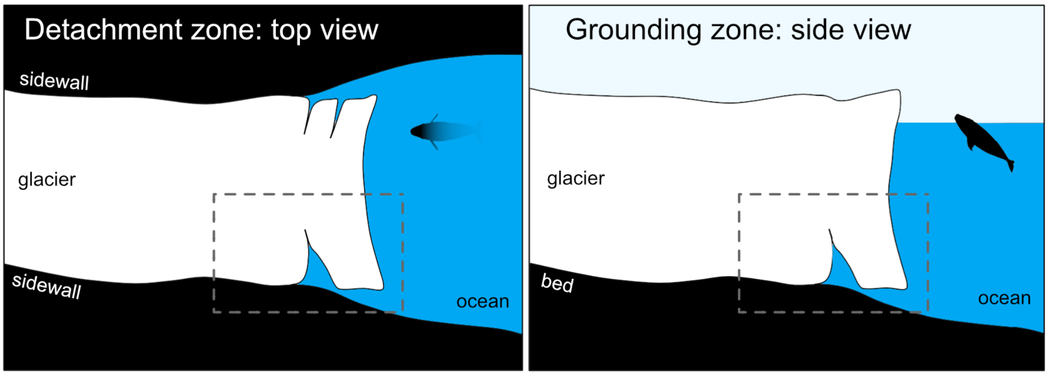

Figure 8. Left: Sketch of a typical detachment zone. Right: Sketch of a typical grounding zone, similar to that depicted in Figure 11 of Murray et al. (2015).

high longitudinal tension should emerge near the base of a glacier through its grounding zone – perhaps tension sufficient to open basal crevasses. Once a crevasse is initiated, buoyant forces could aid in rotating a nascent iceberg outward, encouraging further rift growth, and, ultimately, slab capsize calving.

5 Concluding remarks

The rifts that emerge through detachment zones are a primary mechanism by which ice shelves calve. We have demonstrated that a longitudinal decrease in sidewall friction can produce tension sufficient to explain these rifts. The tension is the result of the spatial transition from a confined flow regime to an unconfined regime. We suggest the steadiness of detachment zone location be considered a key metric for assessing the imminence of dynamic changes to ice shelf flow. For example, the formation of a new detachment zone, or the upstream migration of an existing detachment zone, can both reduce buttressing and induce rifts in new locations of a shelf (Figure 6). Additionally, a shift in rift orientation upstream of detachment zones may indicate enhanced vulnerability of a shelf to reduced buttressing (see Section 4.2.1). To predict these sorts of changes to detachment zones, it will be necessary to model them in more detail than we have in this exploratory study.

A more complete approach to modeling detachment zones will likely require coupling ice shelf dynamics with atmospheric and oceanographic forcing, alongside a better understanding of the means by which a sidewall imparts drag. The position of a detachment zone may, for example, depend on ocean-induced melt beneath shear margins reducing the area of ice-sidewall contact. While we have prescribed a spatially variable friction coefficient to simulate detachment zones, a natural starting point for further analysis would be to explicitly couple shear zone thickness with sidewall resistance.

Acknowledgments

We would like to thank Daniel Shapero and Benjamin Oswald for assistance getting started with icepack, and Karen Alley for the suggestion that detachment zone formation may be linked with the formation of basal channels in shear margins. This work was funded by grants 1716865 and 1933105 from the U.S. National Science Foundation, and grant 80NSSC18K1477 from NASA.

Open research

The code used to produce our detachment zone simulations is available for download at the URL below.

Miele, C. (2022). detachment_zone_notebook [Software]. Zenodo. `https://doi.org/10.5281/zenodo.6388470`

References

Albrecht, T., & Levermann, A. (2012). Fracture field for large-scale ice dynamics. *Journal of Glaciology*, *58*(207), 165–176. doi: 10.3189/2012JoG11J191

Alley, K. E., Scambos, T. A., Alley, R. B., & Holschuh, N. (2019). Troughs developed in ice-stream shear margins precondition ice shelves for ocean-driven breakup. *Science Advances*, *5*(10), 1–8. doi: 10.1126/sciadv.aax2215

Amundson, J. M., Truffer, M., Lüthi, M. P., Fahnestock, M., West, M., & Motyka, R. J. (2008). Glacier , fjord , and seismic response to recent large calving events , Jakobshavn Isbræ , Greenland. , *35*, 2–6. doi: 10.1029/2008GL035281

An, L., Rignot, E., Wood, M., Willis, J. K., Mouginot, J., & Khan, S. A. (2021). Ocean melting of the Zachariae Isstrøm and nioghalvfjerdsfjorden glaciers, northeast Greenland. *Proceedings of the National Academy of Sciences of the United States of America*, *118*(2), 1–8. doi: 10.1073/pnas.2015483118

Bamber, J. L., Oppenheimer, M., Kopp, R. E., Aspinall, W. P., & Cooke, R. M. (2019). Ice sheet contributions to future sea-level rise from structured expert judgment. *Proceedings of the National Academy of Sciences of the United States of America*, *166*(23), 11195–11200. doi: 10.1073/pnas.1817205116

Banwell, A. F., MacAyeal, D. R., & Sergienko, O. V. (2013). Breakup of the Larsen B Ice Shelf triggered by chain reaction drainage of supraglacial lakes. *Geophysical Research Letters*, *40*(22), 5872–5876. doi: 10.1002/2013GL057694

Benn, D. I., & Åström, J. A. (2018). Calving glaciers and ice shelves. *Advances in Physics: X*, *3*(1), 1048–1076. Retrieved from `https://doi.org/10.1080/23746149.2018.1513819` doi: 10.1080/23746149.2018.1513819

Benn, D. I., Warren, C. R., & Mottram, R. H. (2007). Calving processes and the dynamics of calving glaciers. *Earth-Science Reviews*, *82*(3-4), 143–179. doi: 10.1016/j.earscirev.2007.02.002

Cai, C., Rignot, E., Menemenlis, D., & Nakayama, Y. (2017). Observations and modeling of ocean-induced melt beneath Petermann Glacier Ice Shelf in northwestern Greenland. *Geophysical Research Letters*, *44*(16), 8396–8403. doi: 10.1002/2017GL073711

Carroll, D., Sutherland, D. A., Hudson, B., Moon, T., Catania, G. A., Shroyer, E. L., … van den Broeke, M. R. (2016). The impact of glacier geometry on meltwater plume structure and submarine melt in Greenland fjords. *Geophysical Research Letters*, *43*(18), 9739–9748. doi: 10.1002/2016GL070170

Colgan, W., Rajaram, H., Abdalati, W., McCutchan, C., Mottram, R., Moussavi, M., & Grigsby, S. (2016). Glacier crevasses: Observations, models, and mass balance implications. *Reviews of Geophysics*, *54*, 119–161. doi: 10.1002/2017RG000559

Cuffey, K. M., & Paterson, W. S. B. (2010). *The Physics of Glaciers* (4th ed.). Burlington, MA: Butterworth-Heinemann. doi: 10.3189/002214311796405906

Dawson, G. J., & Bamber, J. L. (2020). Measuring the location and width of the Antarctic grounding zone using CryoSat-2. *Cryosphere*, *14*(6), 2071–2086. doi: 10.5194/tc-14-2071-2020

De Rydt, J., Hilmar Gudmundsson, G., Nagler, T., & Wuite, J. (2019). Calving cycle of the Brunt Ice Shelf, Antarctica, driven by changes in ice shelf geometry. *Cryosphere*, *13*(10), 2771–2787. doi: 10.5194/tc-13-2771-2019

De Rydt, J., Hilmar Gudmundsson, G., Nagler, T., Wuite, J., & King, E. C. (2018). Recent rift formation and impact on the structural integrity of the Brunt Ice Shelf, East Antarctica. *Cryosphere*, *12*(2), 505–520. doi: 10.5194/tc-12-505-2018

Enderlin, E. M., & Bartholomaus, T. C. (2020). Sharp contrasts in observed and modeled crevasse patterns at Greenland's marine terminating glaciers. *Cryosphere*, *14*(11), 4121–4133. doi: 10.5194/tc-14-4121-2020

Feldmann, J., Reese, R., Winkelmann, R., & Levermann, A. (2022). Shear-margin melting causes stronger transient ice discharge than ice-stream melting in idealized simulations. *Cryosphere*, *16*(5), 1927–1940. doi: 10.5194/tc-16-1927-2022

Fox-Kemper, B., Hewitt, H. T., Xiao, C., Aalgeirsdóttir, G., Drijfhout, S. S., Edwards, T. L., … Yu, Y. (2021). Ocean, Cryosphere and Sea Level Change. In V. Masson-Delmotte et al. (Eds.), *Climate Change 2021: The Physical Science Basis. Contribution of Working Group I to the Sixth Assessment Report of the Intergovernmental Panel on Climate Change.* Cambridge University Press.

Fürst, J. J., Durand, G., Gillet-Chaulet, F., Tavard, L., Rankl, M., Braun, M., & Gagliardini, O. (2016). The safety band of Antarctic ice shelves. *Nature Climate Change*, *6*(5), 479–482. doi: 10.1038/nclimate2912

Goldberg, D. N., Little, C. M., Sergienko, O. V., Gnanadesikan, A., Hallberg, R., & Oppenheimer, M. (2012). Investigation of land ice-ocean interaction with a fully coupled ice-ocean model: 2. Sensitivity to external forcings. *Journal of Geophysical Research: Earth Surface*, *117*(2), 1–11. doi: 10.1029/2011JF002247

Gudmundsson, G. H. (2013). Ice-shelf buttressing and the stability of marine ice sheets. *The Cryosphere*, *7*(2), 647–655. doi: 10.5194/tc-7-647-2013

Gudmundsson, G. H., Paolo, F. S., Adusumilli, S., & Fricker, H. A. (2019). Instantaneous Antarctic ice sheet mass loss driven by thinning ice shelves. *Geophysical Research Letters*, *46*(23), 13903–13909. doi: 10.1029/2019GL085027

Hill, E. A., Carr, J. R., & Stokes, C. R. (2017). A review of recent changes in major marine-terminating outlet glaciers in northern Greenland. *Frontiers in Earth Science*, *4*(January), 1–23. doi: 10.3389/feart.2016.00111

Hill, E. A., Rachel Carr, J., Stokes, C. R., & Hilmar Gudmundsson, G. (2018). Dynamic changes in outlet glaciers in northern Greenland from 1948 to 2015. *Cryosphere*, *12*(10), 3243–3263. doi: 10.5194/tc-12-3243-2018

Hindmarsh, R. C. (2012). An observationally validated theory of viscous flow dynamics at the ice-shelf calving front. *Journal of Glaciology*, *58*(208), 375–387. doi: 10.3189/2012JoG11J206

Holdsworth, G. (1974). Erebus Glacier Tongue, Mcmurdo Sound, Antarctica. *Journal of Glaciology*, *13*(67), 27–35. doi: 10.3189/s0022143000023340

Holland, D. M., Thomas, R. H., De Young, B., Ribergaard, M. H., & Lyberth, B. (2008). Acceleration of Jakobshavn Isbr triggered by warm subsurface ocean waters. *Nature Geoscience*, *1*(10), 659–664. doi: 10.1038/ngeo316

Hulbe, C. L., LeDoux, C., & Cruikshank, K. (2010). Propagation of long fractures in the Ronne Ice Shelf, Antarctica, investigated using a numerical model of fracture propagation. *Journal of Glaciology*, *56*(197), 459–472. doi: 10.3189/002214310792447743

James, T. D., Murray, T., Selmes, N., Scharrer, K., & O'Leary, M. (2014). Buoyant flexure and basal crevassing in dynamic mass loss at Helheim Glacier. *Nature Geoscience*, *7*(8), 593–596. doi: 10.1038/ngeo2204

Jordan, J. R., Holland, P. R., Goldberg, D., Snow, K., Arthern, R., Campin, J. M., … Jenkins, A. (2018). Ocean-Forced Ice-Shelf Thinning in a Synchronously Coupled Ice-Ocean Model. *Journal of Geophysical Research: Oceans*, *123*(2), 864–882. doi: 10.1002/2017JC013251

Joughin, I., Abdalati, W., & Fahnestock, M. (2004). Large fluctuations in speed on

Greenland's Jakobshavn Isbræ glacier. *Nature*, *432*(7017), 608–610. doi: 10.1038/nature03130

Joughin, I., Shapero, D., Smith, B., Dutrieux, P., & Barham, M. (2021). Ice-shelf retreat drives recent Pine Island Glacier speedup. *Science Advances*, *7*(24), 1–7. doi: 10.1126/sciadv.abg3080

Korsgaard, N. J., Nuth, C., Khan, S. A., Kjeldsen, K. K., Bjørk, A. A., Schomacker, A., & Kjær, K. H. (2016). Digital elevation model and orthophotographs of Greenland based on aerial photographs from 1978-1987. *Scientific Data*, *3*, 1–15. doi: 10.1038/sdata.2016.32

Larour, E., Rignot, E., Poinelli, M., & Scheuchl, B. (2021). Physical processes controlling the rifting of Larsen C Ice Shelf, Antarctica, prior to the calving of iceberg A68. *Proceedings of the National Academy of Sciences*, *118*(40), e2105080118. doi: 10.1073/pnas.2105080118

Lea, J. M. (2018). The Google Earth Engine Digitisation Tool (GEEDiT) and the Margin change Quantification Tool (MaQiT) ndash; Simple tools for the rapid mapping and quantification of changing Earth surface margins. *Earth Surface Dynamics*, *6*(3), 551–561. doi: 10.5194/esurf-6-551-2018

Lhermitte, S., Sun, S., Shuman, C., Wouters, B., Pattyn, F., Wuite, J., … Nagler, T. (2020). Damage accelerates ice shelf instability and mass loss in Amundsen Sea Embayment. *Proceedings of the National Academy of Sciences of the United States of America*, *117*(40), 24735–24741. doi: 10.1073/pnas.1912890117

Lipovsky, B. P. (2020). Ice shelf rift propagation: Stability, three-dimensional effects, and the role of marginal weakening. *Cryosphere*, *14*(5), 1673–1683. doi: 10.5194/tc-14-1673-2020

MacAyeal, D. R. (1989). Large-scale ice flow over a viscous basal sediment: theory and application to Ice Stream B, Antarctica. *Journal of Geophysical Research*, *94*(B4), 4071–4087.

Motyka, R. J., Truffer, M., Fahnestock, M., Mortensen, J., Rysgaard, S., & Howat, I. (2011). Submarine melting of the 1985 Jakobshavn Isbræ floating tongue and the triggering of the current retreat. *Journal of Geophysical Research: Earth Surface*, *116*(1), 1–17. doi: 10.1029/2009JF001632

Mouginot, J., Rignot, E., Scheuchl, B., Wood, M., & Romain, M. (2019). *Annual Ice Velocity of the Greenland Ice Sheet (2010-2017).* Dryad. Retrieved from `https://doi.org/10.7280/D11H3X`

Murray, Aspey, R., Rutt, I., Nettles, M., & Baugé, T. (2015). Dynamics of glacier calving at the ungrounded margin of Helheim GLacier, southeast Greenland. *Journal of Geophysical Research: Earth Surface*, *120*, 534–563. doi: 10.1002/2015JF003531

Nye, J. F. (1955). Comments on Dr. Loewe's Letter and Notes on Crevasses. *Notes*, *2*(17), 512–514.

O'Leary, M., & Christoffersen, P. (2013). Calving on tidewater glaciers amplified by submarine frontal melting. *Cryosphere*, *7*(1), 119–128. doi: 10.5194/tc-7-119-2013

Paolo, F. S., Fricker, H. A., & Padman, L. (2015). Volume loss from Antarctic ice shelves is accelerating. *Science*, *348*(6232), 327–331. doi: 10.1126/science.aaa0940

Reeh, N., Thomsen, H. H., Higgins, A. K., & Weidick, A. (2001). Sea ice and the stability of north and northeast Greenland floating glaciers. *Annals of Glaciology*, *33*, 474–480. doi: 10.3189/172756401781818554

Robel, A. A., Seroussi, H., & Roe, G. H. (2019). Marine ice sheet instability amplifies and skews uncertainty in projections of future sea-level rise. *Proceedings of the National Academy of Sciences of the United States of America*, *116*(30), 14887–14892. doi: 10.1073/pnas.1904822116

Rückamp, M., Neckel, N., Berger, S., Humbert, A., & Helm, V. (2019). Calving Induced Speedup of Petermann Glacier. *Journal of Geophysical Research: Earth Surface*, *124*(1), 216–228. doi: 10.1029/2018JF004775

Schoof, C. (2007). Ice sheet grounding line dynamics: Steady states, stability, and hysteresis. *Journal of Geophysical Research: Earth Surface*, *112*(3). doi: 10.1029/2006JF000664

Shapero, D. R., Badgeley, J. A., Hoffman, A. O., & Joughin, I. R. (2021). Icepack: A new glacier flow modeling package in Python, version 1.0. *Geoscientific Model Development*, *14*(7), 4593–4616. doi: 10.5194/gmd-14-4593-2021

Todd, J., Christoffersen, P., Zwinger, T., Råback, P., Chauché, N., Benn, D., ... Hubbard, A. (2018). A Full-Stokes 3-D Calving Model Applied to a Large Greenlandic Glacier. *Journal of Geophysical Research: Earth Surface*, *123*(3), 410–432. doi: 10.1002/2017JF004349

Tsai, V. C., Stewart, A. L., & Thompson, A. F. (2015). Marine ice-sheet profiles and stability under Coulomb basal conditions. *Journal of Glaciology*, *61*(226), 205–215. doi: 10.3189/2015JoG14J221

van der Veen, C. J. (2013). *Fundamentals of Glacier Dynamics* (2nd ed.). Boca Raton, FL: Taylor and Francis Group.

van der Veen, C. J., Plummer, J. C., & Stearns, L. A. (2011). Controls on the recent speed-up of Jakobshavn Isbræ, West Greenland. *Journal of Glaciology*, *57*(204), 770–782. doi: 10.3189/002214311797409776

Veitch, S. A., & Nettles, M. (2012). Spatial and temporal variations in Greenland glacial-earthquake activity, 1993-2010. *Journal of Geophysical Research: Earth Surface*, *117*(4), 1993–2010. doi: 10.1029/2012JF002412

Vieli, A., Payne, A. J., Du, Z., & Shepherd, A. (2006). Numerical modelling and data assimilation of the Larsen B ice shelf, Antarctic Peninsula. *Philosophical Transactions of the Royal Society A: Mathematical, Physical and Engineering Sciences*, *364*(1844), 1815–1839. doi: 10.1098/rsta.2006.1800

Wagner, T. J., James, T. D., Murray, T., & Vella, D. (2016). On the role of buoyant flexure in glacier calving. *Geophysical Research Letters*, *43*(1), 232–240. doi: 10.1002/2015GL067247

Wearing, M. G., Kingslake, J., & Worster, M. G. (2020). Can unconfined ice shelves provide buttressing via hoop stresses? *Journal of Glaciology*, *66*(257), 349–361. doi: 10.1017/jog.2019.101

Weertman, J. (1957). Deformation of floating ice shelves. *Journal of Glaciology*, *3*(21).

Winberry, J. P., Huerta, A. D., Anandakrishnan, S., Aster, R. C., Nyblade, A. A., & Wiens, D. A. (2020). Glacial Earthquakes and Precursory Seismicity Associated With Thwaites Glacier Calving. *Geophysical Research Letters*, *47*(3), 1–7. doi: 10.1029/2019GL086178

Supporting Information for "Marginal detachment zones: the fracture factories of ice shelves?"

Chris Miele [1], Timothy C. Bartholomaus [1], Ellyn M. Enderlin [2]

[1]Department of Geological Sciences, University of Idaho, Moscow, ID, USA

[2]Department of Geosciences, Boise State University, Boise, ID, USA

Contents of this file

Additional Supporting Information (Files uploaded separately)

Introduction Text S1 describes three finite element simulations wherein "simple" detachment zones are modeled by imposing three different boundary condition transitions. These are a) continuously diminishing marginal friction, as discussed in the main text, b) an abrupt transition from no-slip sidewalls to laterally unconfined margins, and c) an abrupt transition from no-slip sidewalls to free-slip sidewalls. Text S2 describes a finite element simulation wherein ice rise detachment is treated as a basal process, rather than the lateral process discussed in the main text. Figure S1 illustrates the comparison dis-

Corresponding author: Chris Miele, Department of Geological Sciences, University of Idaho, Moscow, ID, USA. (miel4255@vandals.uidaho.edu)

cussed in Text S1. Figure S2 illustrates the setup described in Text S2. Movie S1 shows the evolution of detachment zones at 79 North from 1984 to 2019. Movie S2 shows the propagation of detachment rifts at C. H. Ostenfeld, from 1985, and captures the collapse of the ice tongue in the early 2000s and the subsequent shift in rifting and calving behaviour. Movie S3 captures the formation of detachment rifts at one of the small ice tongues off Zachariae's ice shelf from 1984 to 2003. Movie S4 documents the propagation of detachment rifts, and subsequent calving events, experienced by Ryder Glacier between 1999 and 2019.

Text S1.

In the main text, we model simple detachment zones (as in Figure 3) by imposing a spatially variable sidewall friction coefficient at the sidewalls. Here, we show two other types of transition in marginal boundary conditions.

Setup for the experiments described below is the same as that described in Section 2.2.1 for C. H. Ostenfeld, except for the marginal boundary conditions.

To provide a baseline for the two additional experiments, we first reproduce the experiment which produced Figure 3, but with baseline coefficient of friction $C_0 = 0.1$ rather than $C_0 = 0.05$. This also demonstrates that results are not particularly sensitive to small variations in C_0.

For the first additional experiment, we allow the shelf to become laterally unconfined after sidewall detachment. To model this situation, we impose an abrupt transition in marginal boundary condition, halfway down the length of the domain. Before the 5 km mark, the lateral boundaries are no-slip sidewalls. After the 5 km mark, the lateral boundaries are terminus-type boundaries, which spread outward at a rate proportional to their thickness.

For the second additional experiment, we allow the shelf to abruptly begin to slip against its margins, as opposed to gradually losing resistance (as described in the main text). In this simulation, before the 5 km mark, the lateral boundaries are no-slip sidewalls; after the 5 km mark, the lateral boundaries are free-slip sidewalls.

In both additional cases, we solve the SSA iteratively toward a steady state, as described in the main text. Results, which are depicted in Figure S1, indicate that key qualitative findings (the visible transition in flow regime, the surface elevation profile, and the location of rifting) are robust to choice of boundary condition type.

Text S2.

We have described, in the main text, the process by which flow between ice rises can be described in terms of lateral resistance. However, ice rises impart basal drag directly, and lateral drag only indirectly. Therefore, we include an experiment which treats ice rises as providing basal resistance, and we show that this setup does not change the qualitative nature of our findings.

In this experiment, the initial geometry of the shelf 5 km wide by 8 km long, with uniform surface elevation of 10 m. The domain is somewhat larger than that chosen to produce Figure 4, because we now include flow over the ice rises (which were not part of the domain in Figure 4). We provide a geometric description of the bed beneath the shelf, with two bedrock bumps protruding upward into the base of the shelf (see panels c and d of Figure S2). Where there is any contact between the shelf base and the bedrock, the coefficient of basal friction scales with height above flotation (which must be positive where the shelf is locally grounded), to a maximum value of $C_0 = 0.1$. We solve the Shallow Stream Approximation iteratively toward a steady state. Results are depicted in Figure S2. We find that the resulting velocity field, surface elevation profile, and rift locations are qualitatively similar to results in the main text.

Movie S1.

Timelapse sequence of two protruding tongues at 79 North, the lower of which is modeled in the main text. Images span from 1984 to 2019. The margins of the tongues are manually delineated briefly in a 1997 image, just prior to a major calving event. Detachment rifts open periodically from the ice rises and cut inward and slightly upstream.

Movie S2.

Timelapse sequence of C. H. Ostenfeld from 1985 to 2006. Besides illustrating the propagation of detachment rifts from the glacier's right margin, this sequence also captures the breakup of the tongue in the early 2000s. Upon transitioning into a nearly-grounded regime, C. H. Ostenfeld no longer produces detachment rifts. While the tongue persists, a black dot is drawn as a visual aid.

Movie S3.

Timelapse sequence of a small ice tongue to the east of Zachariae's main shelf. The time range spans from 1984 to 2003, at which point Zachariae's main shelf (not visible in this frame) collapses, decoupling from the region depicted. Beyond 2003, flow almost entirely halts at the tongue shown. For the duration shown, detachment rifts can be seen propagating inward from the island at the right.

Movie S4.

Timelapse sequence of Ryder Glacier from 1999 to 2019. Detachment rifts form in rapid succession from the left margin (12 are formed over the course of the 20 years shown, as indicated by the numbering depicted), while detachment rifts formed at the right margin are larger and more widely spaced. All major calving events occurring over this time result from detachment rifts at the right propagating across the glacier, ultimately joining the smaller rifts on the left.

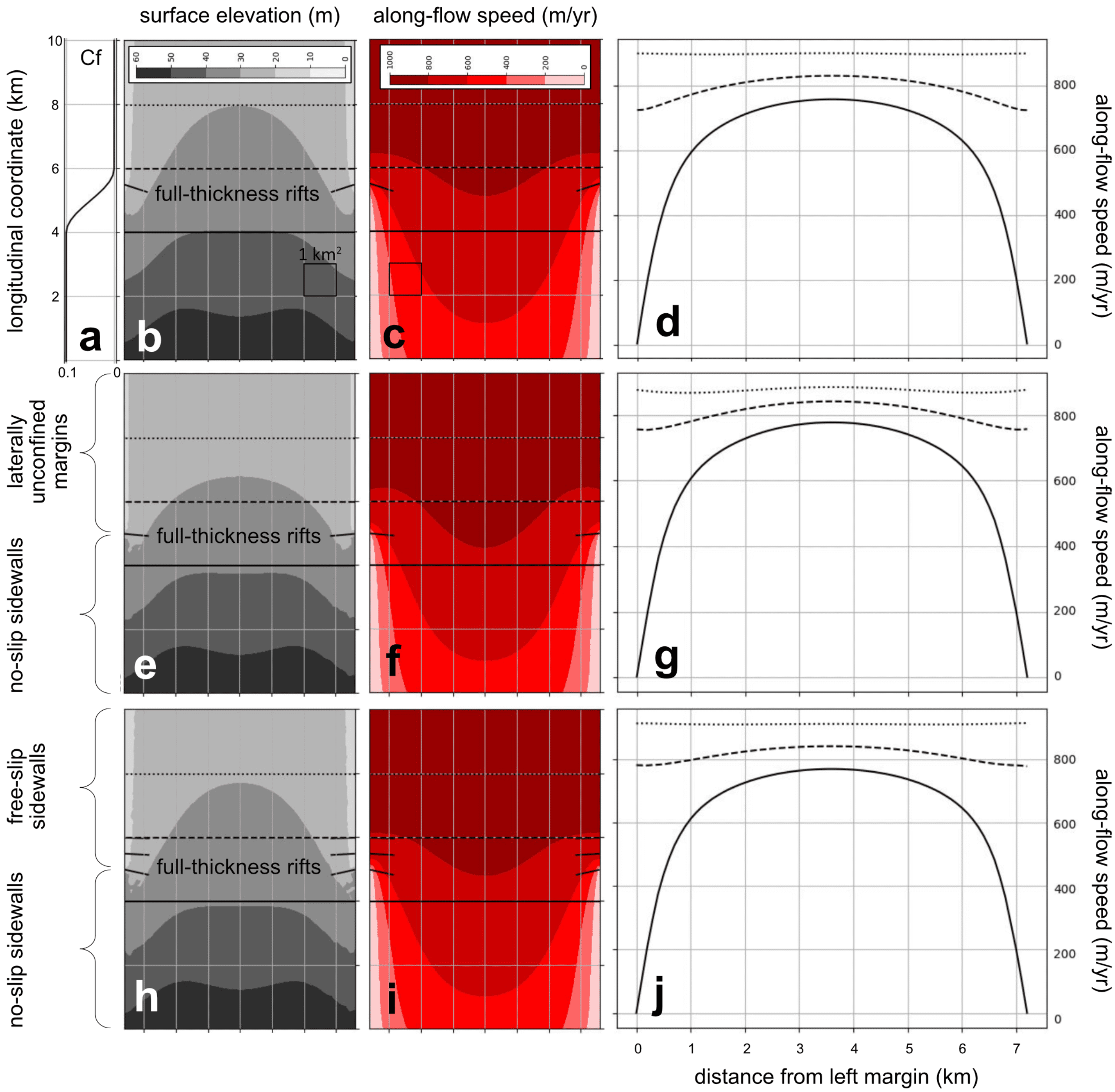

Figure S1. A comparison of three types of boundary condition transition. See Figure 3 in the main text for a description of A through D, which and are duplicated here to permit side-by-side comparisons with the experiments described below. Panels E through G correspond to an experiment wherein no-slip sidewalls transition abruptly to laterally unconfined margins. Panels H through J correspond to an experiment wherein no-slip sidewalls transition abruptly to free-slip sidewalls. B, E, and H depict steady-state surface elevation profiles, C, F, and I depict steady-state velocity profiles, and D, G, and J depict selected velocity transects.

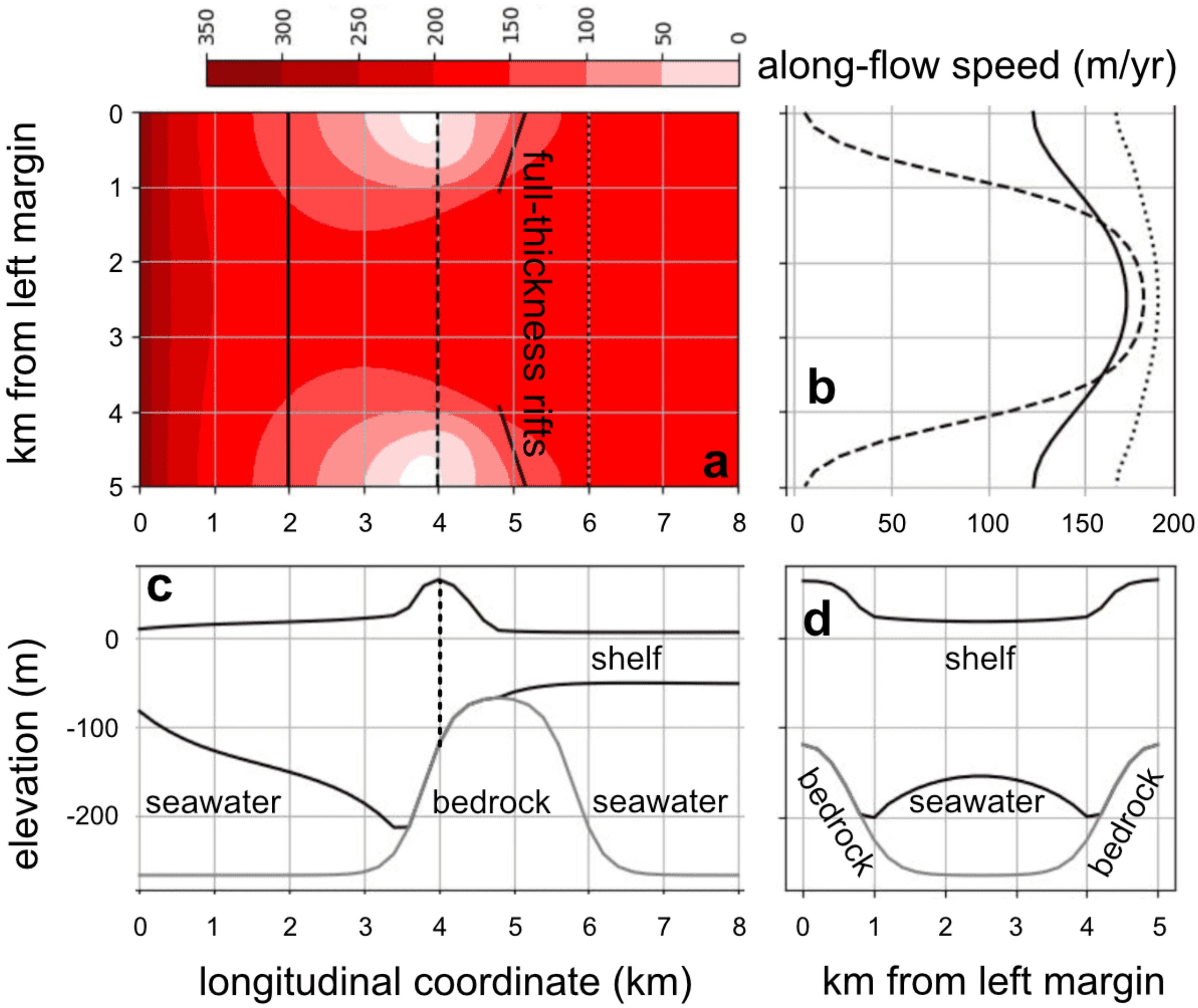

Figure S2. Finite element simulation comparable to that described in Figure 4 in the main text. Here, resistance originates at the base as the shelf flows between two local bedrock highs. Panel A shows the resulting steady-state velocity field. Panel B shows the speed across three lateral transects. C depicts the steady-state geometry of the shelf, as seen from the side. D shows the steady-state geometry of the shelf, as seen from head-on.